Modeling of elasticity effects of sandstone compaction using coated inclusions

Remy Agersborg[1], Tor Arne Johansen[2], Gary Mavko[3], and Tiziana Vanorio[3]

ABSTRACT

Compaction of siliciclastic sediments leads to an increase in their stiffness parameters and seismic velocities. Although mechanical compaction implies a reduction of porosity and closing of compliant pores, chemical compaction may alter the mineral properties, the cementing of grain contacts, and the pore volume. The ability of rock physics models to quantify such effects on seismic observables will aid hydrocarbon exploration. A framework was designed for modeling compaction effects by use of a so-called coated inclusion model that eliminates the need of using a hybrid approach through combining different theories. A basic feature of the model is that the inclusion is defined by a kernel representing the pore, which is surrounded by shells that may individually have different elastic properties from those of the pore-filling material and the background matrix. The modeling can be designed to explore seismic effects of various texture perturbations, including contact cementing and pore-filling processes. The numerical modelings seem to be consistent with the results obtained from other rock physics models. The model allows for the possibility of including small-scale heterogeneities within the rock texture and estimating frequency dispersion together with attenuation due to pore fluid flow. A basic weakness of the method is the relatively large number of parameters needed to describe a porous rock, which will always limit its practical usage. However, its basic physical foundation may provide a reference for understanding the qualitative and quantitative effects of various cementation scenarios on seismic parameters.

INTRODUCTION

Quantification of the effects of deposition and compaction of sediment on the elastic properties usually helps to improve seismic interpretation for lithology and fluid. Compaction means mechanical loading due to burial as well as cementation (or lithification) due to geochemical reactions. Compaction is affected by the sediment composition at the time of deposition, time history of pressure and temperature, and the influence of adjacent rock, such as calcite-rich sediment (e.g., Avseth et al., 2005).

Numerous models have been developed to predict compaction effects on the elastic and seismic properties of porous rocks. A comprehensive review of various models considered for use can be found in Mavko et al. (2009). Dvorkin et al. (1994) and Dvorkin and Nur (1996) show that the location of the cement within the pore space, rather than the amount of cement, governs the stiffness effect. For instance, adding only a small amount of cement on the grain contacts of an unconsolidated rock increases its elastic moduli strongly. On the contrary, pore-filling clay hardly influences the elastic moduli.

While mechanical compaction dominates for shallow sediments, chemical compaction starts to dominate at larger depths; for example, in North Sea siliciclastics, quartz cementation starts at approximately 2-km depth (Avseth et al. 2005; Dræge et al. 2006a). Temperature is a key factor for such chemical processes to take place, and various mineral compositions may have different temperature intervals in which the transition from being chemically unstable to stable occurs. Furthermore, the various cement types may precipitate differently in the pore space (e.g., as a grain coating, at grain contacts, or as pore bridging, etc.).

Dræge et al. (2006a,b) discussed the role of mineral transitions due to diagenesis and the influence of grain-scale cement distribution on the seismic properties. The modeling in this work was performed by using various rock physics models

depending on the degree of cementation. For instance, at the time of deposition, the sediment was modeled using contact theories. In contrast, with increasing depth and onset of cementation, the contact cement theory (CCT) (Dvorkin and Nur, 1996) was used. To address the effects of large amounts of cement on the elastic properties, inclusion models were utilized.

Avseth et al. (2005) also describe how the change in seismic attributes relates to effects caused by deposition and compaction: Whereas compaction may cause a relatively small change in porosity but a large increase in seismic velocities, depositional phenomena (e.g., sorting and grain size) may alter the porosity, but only gently affect the velocities.

The need for several rock physics models, with their different assumptions and limitations when modeling diagenetic trends, may not always be satisfactory. Whereas mechanical compaction is discussed in Jakobsen and Johansen (2005), we here introduce an extension of the effective medium model described by Jakobsen et al. (2003a,b) and Jakobsen and Johansen (2005). It is designed to avoid the need for moving from one rock physics model to another as the rock texture and cementation alter with compaction. We refer to it as a coated inclusion model (CIM), in which various diagenetic processes are mimicked by various ways of adding/removing cement into/from the pore space represented by inclusions. Path A in Figure 1 illustrates this approach by showing how introducing contact cement dramatically stiffens the rock and hardly causes porosity loss. This can be modeled by gradually adding cement to eventually close the most compliant pores (i.e., inclusions with low aspect ratios). In contrast to path B in Figure 1, the effect of grain sorting, which slightly increases the stiffness at large porosity loss, can be modeled as gradual cementation of the least compliant pores.

Having a single micromechanical model to capture a wide range of geological processes affecting the seismic properties of rocks has the following additional advantages:

- We can rigorously address velocity-frequency dispersion due to local pore-scale fluid flow and compute the resulting attenuation.

- We can model the effects of pore closure and associated porosity reduction due to mechanical compaction on the elastic properties.
- We can consistently alter mineral properties at the pore scale as it occurs due to diagenesis.

This model has many inputs (depending on the number of inclusion aspect ratios and the degree of cementation in each type of inclusion) to mimic essentially any elastic behavior observed in porous rock. Naturally, this feature turns into a disadvantage because it implies serious nonuniqueness in mimicking data by a model. This situation is not uncommon in rock physics. A way to address it and still arrive at a consistent rock physics model is to calibrate the inputs at one (or a few) data points and then make sure it works well within the remaining data set (e.g., a set of well log data). CIM allows for such data-consistent calibration because it can use a single initial inclusion configuration to cover various compaction processes in a large porosity range. Moreover, CIM can serve to quantify how various diagenetic perturbations affect the elastic properties of rock and, hence, provide guidelines for seismic interpretation of porosity, lithology, and fluid.

Although diagenetic parameters such as temperature and geochemical processes can be implemented in this model framework by altering the cement or mineral properties and/or the distribution of the cement, the main focus in this paper is to present the model framework itself. We start by presenting the geometrical interpretation of coated inclusions and how these can be adapted to describe properties of granular and cemented rocks. Then, the formalism behind the model is thoroughly presented before some numerical examples and the main conclusions are given.

COATED INCLUSIONS MODEL

Similar to other inclusion-based models, we consider a porous system in which the porosity is made up of ellipsoidal pores defined by their aspect ratios and fractions of the bulk volume. The aspect ratio α is defined as the ratio of the smallest to largest axis of an ellipsoid. We organize the inclusions to be characterized by N predefined aspect ratios, where $v^{(r)}$, $r = 1, \ldots, N$ denote the total volume fractions of the various pores. Individual families of inclusions, which have the same properties, are characterized by an aspect ratio of $\alpha^{(r)}$. The orientation of pores with the same aspect ratio and composition can be defined by an orientation distribution function $A^{(r)}$ as outlined in Jakobsen et al. (2003a,b). Alignment of pores generally leads to elastic anisotropy (Sayers and Kachanov, 1995), but this is only briefly reviewed in the following.

Consider a granular medium of grains in contact as illustrated in Figure 2, similar to the one used for the derivation of the contact cement model by Dvorkin and Nur (1996). We let the porosity constituted by the void space close to the grain contacts be represented by empty low aspect ratio inclusions, which are elastically very compliant. The remaining stiffer void space is associated with spherical pores with $\alpha = 1$. If grains are cemented around their contact points, we define the material within the smallest aspect ratio inclusions to have the elastic properties of the considered cement (clay, quartz, etc.). As further cementation (or mechanical compaction) occurs, the aspect ratios and material properties of the pore system can be altered
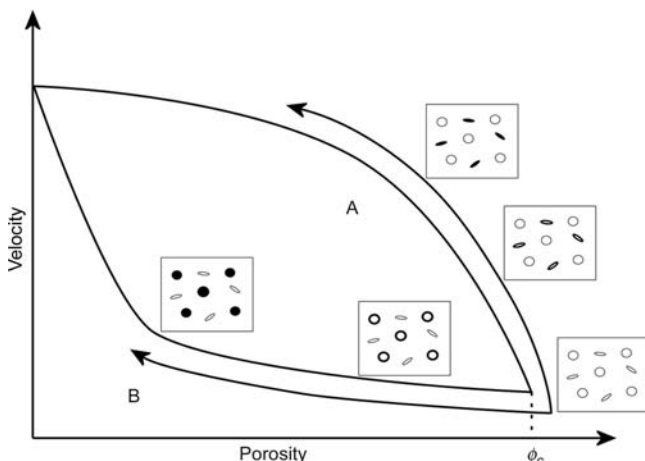

Figure 1. Conceptual picture of the velocity trends due to different distributions of cement in pores. Path A: the cement is precipitated in grain contacts first. Path B: the cement is precipitated in the voids first.

accordingly. The pores can be connected or isolated with respect to pore fluid flow.

We may now also infer cementation to occur at the pore walls (which may gradually fill the pore) by implementing coated inclusions. Such inclusions may be defined to contain k layers of shells surrounding a kernel as illustrated in Figure 3. In this implementation, the surfaces of the layers are ellipsoidal in shape and the principal axes of all of the surfaces coincide. In this paper, we limit ourselves to consider only pores having one shell (cement) and one kernel (empty or fluid-filled pore). The aspect ratio of the kernel, which describes the geometry of the interface between the pore and the cement within it, can be arbitrary ($\alpha \leq 1$), depending on the amount of cement and where it is precipitated. If the cement is precipitated evenly around the pore, the aspect ratio of the kernel is simply the aspect ratio of the inclusion itself. If the cement is precipitated at the grain contacts (i.e., within the compliant pores) the aspect ratio of the kernel increases and may approach one. When the amount of cement is changing, we simply change the relative concentration of the shell/coating inside of each inclusion, as depicted in Figure 4.

MODELING OF A MULTICOATED INCLUSION MODEL USING THE T-MATRIX APPROACH

The modeling follows a two-step procedure in which the first step is to obtain the elastic properties of a local domain of the matter in which inclusions are considered to be aligned. The second step is to model the overall elastic properties from an orientation distribution function of the inclusion geometries (i.e., $A^{(r)}$). Various procedures for obtaining the second step can be found in Johansen et al. (2004). In the following, we discuss step 1 because this is the main result of the paper. As a basis, we use the so-called T-matrix formalism for the modeling of an effective viscoelastic medium described in Jakobsen et al. (2003a,b). It considers pores as aligned ellipsoidal inclusions embedded in a medium characterized by a fourth-rank stiffness tensor $\mathbf{C}^{(0)}$. The resulting effective stiffness tensor $\mathbf{C}^*$ can be expressed by

$$\mathbf{C}^* = \mathbf{C}^{(0)} + \mathbf{C}_1 : (\mathbf{I}_4 + \mathbf{C}_1^{-1} : \mathbf{C}_2)^{-1}, \qquad (1)$$

where

$$\mathbf{C}_1 = \sum_{r=1}^{N} v^{(r)} \mathbf{t}^{(r)}, \qquad (2)$$

and

$$\mathbf{C}_2 = \sum_{r=1}^{N} \sum_{s=1}^{N} v^{(r)} \mathbf{t}^{(r)} : \mathbf{G}_d^{(rs)} : \mathbf{t}^{(s)} v^{(s)}. \qquad (3)$$

Here, $\mathbf{I}_4$ is the identity for the fourth-rank tensor and $\mathbf{t}^{(r)}$ is the t-matrix for the inclusions of family r. $\mathbf{G}_d^{(rs)}$ is given by the strain Green's functions integrated over a characteristic ellipsoid having the same symmetries as $p^{(s|r)}(\pmb{x}\text{-}\pmb{x}')$ which, in turn, gives the probability density for finding an inclusion of type s at point $\pmb{x}'$ given there is an inclusion of type r at point $\pmb{x}$.

In this approach, the inclusion with the same properties (i.e., stiffness tensor, concentration, shape, and orientation) can be characterized by one t-matrix and these t-matrices are regarded as empty or completely filled with a material or a fluid. In this paper, we extend the formalism of Jakobsen et al. (2003a,b) and Jakobsen and Chapman (2009) to also include inclusions containing a kernel surrounded by k shells. The kernel and each shell are characterized by a unique stiffness tensor based on the material properties in each layer.

Jakobsen et al. (2003a,b) related the stress $\pmb{\sigma}^{(0)}$ at an external surface to the strain within a nonlayered inclusion r, $\pmb{\varepsilon}^{(r)}$, containing a material with properties $\mathbf{C}^{(r)}$ as
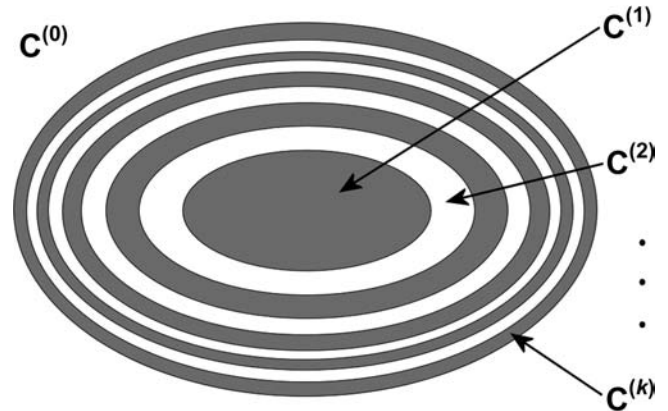
Figure 3. Geometry of a multicoated inclusion with one kernel and $k - 1$ shells.
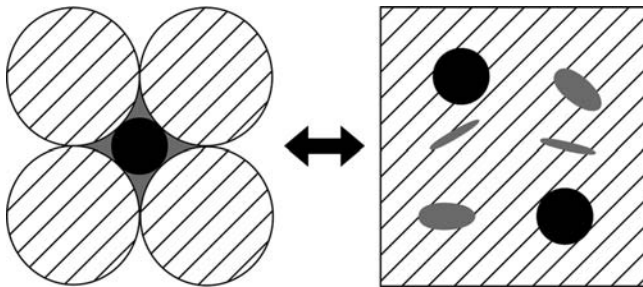

Figure 2. Conceptual picture of porosity of a spherical grain packing and the equivalent effective medium model. The gray part of the porosity corresponds to pores of aspect ratios <1, whereas the black part corresponds to pores of aspect ratio equal to one.
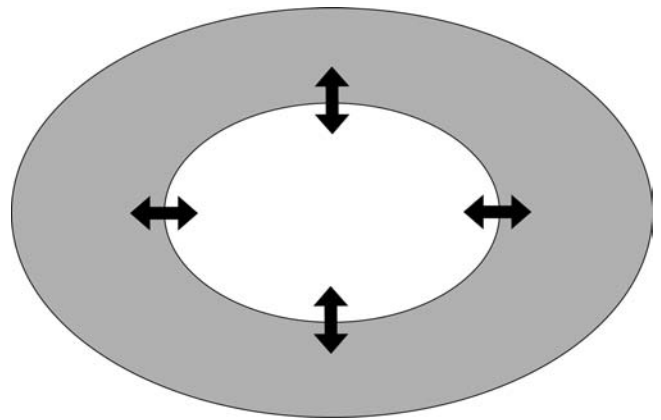

Figure 4. Cement content is growing or declining dependent on whether it precipitates at or dissolves from the pore wall.

$$\boldsymbol{\varepsilon}^{(r)} = \mathbf{K}^{(r)} : \boldsymbol{\sigma}^{(0)}, \tag{4}$$

where

$$\mathbf{K}^{(r)} = [\mathbf{I}_4 - \mathbf{G}^{(r)} : (\mathbf{C}^{(r)} - \mathbf{C}^{(0)})]^{-1} : \mathbf{S}^{(0)}. \tag{5}$$

Here, $\mathbf{S}^{(0)} = (\mathbf{C}^{(0)})^{-1}$ and $\mathbf{G}^{(r)}$ is the Green's tensor for the inclusions of type r. The t-matrix for a single inclusion of type r is given by (Jakobsen et al., 2003a,b)

$$\mathbf{t}^{(r)} = (\mathbf{C}^{(r)} - \mathbf{C}^{(0)}) : [\mathbf{I}_4 - \mathbf{G}^{(r)} : (\mathbf{C}^{(r)} - \mathbf{C}^{(0)})]^{-1}. \tag{6}$$

Now, suppose the inclusion is a multicoated inclusion in which the kernel is composed of material characterized by the stiffness tensor $\mathbf{C}^{(1)}$ and the coatings are composed of materials with the stiffness tensors $\mathbf{C}^{(2)},..., \mathbf{C}^{(k)}$, as illustrated in Figure 3. The fluctuation of $\mathbf{C}(\mathbf{x})$ inside of the inclusion of type r from $\mathbf{C}^{(0)}$ will now be $\delta\mathbf{C}^{(r)}$ instead of $(\mathbf{C}^{(r)} - \mathbf{C}^{(0)})$ such that the t-matrix for a single multicoated inclusion of type r is

$$\mathbf{t}^{(r)} = \delta\mathbf{C}^{(r)} : [\mathbf{I}_4 - \mathbf{G}^{(r)} : \delta\mathbf{C}^{(r)}]^{-1}. \tag{7}$$

The fluctuation of stress inside of the inclusion can be expressed as

$$\delta\mathbf{C}^{(r)}(\mathbf{x}) = \sum_{j=1}^{k} (\mathbf{C}^{(j)} - \mathbf{C}^{(0)})\theta_j(\mathbf{x}), \tag{8}$$

where $\theta_j(x)$ is the heaviside step function defined as

$$\theta_j(\mathbf{x}) = \begin{cases} 1 & \text{if } \mathbf{x} \in V_j^{(r)} \\ 0 & \text{if } \mathbf{x} \notin V_j^{(r)} \end{cases}. \tag{9}$$

Here, $V_j^{(r)}$ is the region of coating j and the total region ($V^{(r)}$) of inclusion r is

$$V^{(r)} = \sum_{j=1}^{k} V_j^{(r)}. \tag{10}$$

The average stress difference will be

$$\langle \delta\mathbf{C}^{(r)}(\mathbf{x}) : \boldsymbol{\varepsilon}(\mathbf{x}) \rangle = \delta\mathbf{C}^{(r)} : \boldsymbol{\varepsilon}^{(r)}$$
$$= \frac{1}{|V^{(r)}|} \int_{V^{(r)}} d\mathbf{x} \delta\mathbf{C}^{(r)}(\mathbf{x}) : \boldsymbol{\varepsilon}(\mathbf{x}). \tag{11}$$

Inserting for $\delta\mathbf{C}^{(r)}(\mathbf{x})$ we obtain

$$\delta\mathbf{C}^{(r)} : \boldsymbol{\varepsilon}^{(r)} = \frac{1}{|V^{(r)}|} \int_{V^{(r)}} d\mathbf{x} \sum_{j=1}^{k} (\mathbf{C}^{(j)} - \mathbf{C}^{(0)})\theta_j(\mathbf{x}) : \boldsymbol{\varepsilon}(\mathbf{x})$$
$$= \sum_{j=1}^{k} \frac{|V_j^{(r)}|}{|V^{(r)}|} (\mathbf{C}^{(j)} - \mathbf{C}^{(0)})$$
$$\times \frac{1}{V_j^{(r)}} \int_{V^{(r)}} d\mathbf{x}\theta_j(\mathbf{x}) : \boldsymbol{\varepsilon}(\mathbf{x}). \tag{12}$$

Because the average strain for each coating is

$$\langle \boldsymbol{\varepsilon}_j^{(r)}(\mathbf{x}) \rangle = \boldsymbol{\varepsilon}_j^{(r)} = \frac{1}{|V_j^{(r)}|} \int_{V_j^{(r)}} d\mathbf{x}\boldsymbol{\varepsilon}(x), \tag{13}$$

the average stress difference for an inclusion of type r will be

$$\delta\mathbf{C}^{(r)} : \boldsymbol{\varepsilon}^{(r)} = \sum_{j=1}^{k} \phi_j(\mathbf{C}^{(j)} - \mathbf{C}^{(0)}) : \boldsymbol{\varepsilon}_j^{(r)}. \tag{14}$$

Here, $\varphi_j = V_j^{(r)}/V^{(r)}$ is the relative concentration of coating j and $\sum_j \varphi_j = 1$.

Now, suppose there exists a concentration tensor $\boldsymbol{\beta}^{(j)}$ such that

$$\boldsymbol{\varepsilon}_j^{(r)} = \boldsymbol{\beta}^{(j)} : \boldsymbol{\varepsilon}^{(r)}, \tag{15}$$

then

$$\delta\mathbf{C}^{(r)} : \boldsymbol{\varepsilon}^{(r)} = \left(\sum_{j=1}^{k} \phi_j(\mathbf{C}^{(j)} - \mathbf{C}^{(0)}) : \boldsymbol{\beta}^{(j)} \right) : \boldsymbol{\varepsilon}^{(r)}, \tag{16}$$

and the t-matrix for a multicoated inclusion can be expressed as

$$\mathbf{t}^{(r)} = \left(\sum_{j=1}^{k} \varphi_j(\mathbf{C}^{(j)} - \mathbf{C}^{(0)}) : \boldsymbol{\beta}^{(j)} \right) :$$
$$\left[\mathbf{I}_4 - \mathbf{G}^{(r)} : \left(\sum_{j=1}^{k} \varphi_j(\mathbf{C}^{(j)} - \mathbf{C}^{(0)}) : \boldsymbol{\beta}^{(j)} \right) \right]^{-1}. \tag{17}$$

To find the concentration tensor, we will follow the same procedure as Lipinski et al. (2006), which is reviewed in Appendix A. Notice that if we have no coatings within the inclusion, all of these formulas will reduce to the original t-matrix of a single inclusion.

For drainable inclusions (e.g., communicating multicoated inclusions), we have to extend the equations of Jakobsen et al. (2003b). By inspection of equations 5, 6, and 17, the K-tensor for a multicoated inclusion of type r can be written as

$$\mathbf{K}^{(r)} = \left[\mathbf{I}_4 - \mathbf{G}^{(r)} : \left(\sum_{j=1}^{k} \phi_j(\mathbf{C}^{(j)} - \mathbf{C}^{(0)}) : \boldsymbol{\beta}^{(j)} \right) \right]^{-1} : \mathbf{S}^{(0)}. \tag{18}$$

Because it is in principle possible to track the individual strains within all of the layers in an inclusion, the principle of linear superposition can be applied. Hence,

$$\mathbf{K}^{(r)} : \boldsymbol{\sigma}^{(0)} = \mathbf{K}_d^{(r)} : \left(\boldsymbol{\sigma}^{(0)} + \mathbf{I}_2 : p_f^{(r)} \right) - \mathbf{S}^{(0)} : \mathbf{I}_2 : p_f^{(r)}. \tag{19}$$

Here, $\mathbf{I}_2$ is the second-rank identity tensor and

$$\mathbf{K}_d^{(r)} = \left[\mathbf{I}_4 + \phi_1\mathbf{G}^{(r)} : \mathbf{C}^{(0)} : \boldsymbol{\beta}^{(1)} - \mathbf{G}^{(r)} \right.$$
$$\left. \times \left(\sum_{j=2}^{k} \phi_j(\mathbf{C}^{(j)} - \mathbf{C}^{(0)}) : \boldsymbol{\beta}^{(j)} \right) \right]^{-1} : \mathbf{S}^{(0)}. \tag{20}$$

Using equations 16 and 19, the t-matrix can be expressed by the K-tensor (Jakobsen et al., 2003b):

$$\mathbf{t}^{(r)} = (\mathbf{G}^{(r)})^{-1} : (\mathbf{K}^{(r)} : \mathbf{C}^{(0)} - \mathbf{I}_4). \tag{21}$$

Applying the same procedure as Jakobsen et al. (2003b) using a second-rank tensor $\psi^{(r)}$, which relates the fluid pressure in the rth cavity set to the applied stress,

$$p_f^{(r)} = \psi^{(r)} : \boldsymbol{\sigma}^{(0)}, \tag{22}$$

we get

$$\mathbf{K}^{(r)} = \mathbf{K}_d^{(r)} + (\mathbf{K}_d^{(r)} - \mathbf{S}^{(0)}) : (\mathbf{I}_2 \otimes \psi^{(r)}), \tag{23}$$

$$\mathbf{t}^{(r)} = (\mathbf{G}^{(r)})^{-1} : [(\mathbf{K}_d^{(r)} + (\mathbf{K}_d^{(r)} - \mathbf{S}^{(0)}) : (\mathbf{I}_2 \otimes \psi^{(r)})) : \mathbf{C}^{(0)} - \mathbf{I}_4],$$
(24)

and

$$\mathbf{t}^{(r)} = \mathbf{t}_d^{(r)} + (\mathbf{G}^{(r)})^{-1} : (\mathbf{K}_d^{(r)} - \mathbf{S}^{(0)}) : (\mathbf{I}_2 \otimes \psi^{(r)}) : \mathbf{C}^{(0)},$$
(25)

where

$$\mathbf{t}_d^{(r)} = (\mathbf{G}^{(r)})^{-1} : (\mathbf{K}_d^{(r)} : \mathbf{C}^{(0)} - \mathbf{I}_4)$$
(26)

is the t-matrix of the dry cavity of type r, $\psi^{(r)}$ is the same cavity fluid polarization tensor used by Jakobsen et al. (2003b), and $\otimes$ denotes a dyadic tensor product.

Inserting equation 20 for $\mathbf{K}_d^{(r)}$ into equation 26, we obtain

$$\mathbf{t}_d^{(r)} = \left(-\phi_1 \mathbf{C}^{(0)} : \boldsymbol{\beta}^{(1)} + \left(\sum_{j=2}^{k} \phi_j (\mathbf{C}^{(j)} - \mathbf{C}^{(0)}) : \boldsymbol{\beta}^{(j)} \right) \right) :$$
$$\left[\mathbf{I}_4 + \phi_1 \mathbf{G}^{(r)} : \mathbf{C}^{(0)} : \boldsymbol{\beta}^{(1)} - \mathbf{G}^{(r)} \left(\sum_{j=2}^{k} \phi_j (\mathbf{C}^{(j)} - \mathbf{C}^{(0)}) : \boldsymbol{\beta}^{(j)} \right) \right]^{-1}.$$
(27)

This is consistent with equation 17 and the problem has been reduced to the evaluation of $\psi^{(r)}$. For communicating cavities, we can therefore use the same formulas as in Jakobsen et al. (2003b) with the new expression for $\mathbf{t}_d^{(r)}$ and $\mathbf{K}_d^{(r)}$:

$$\mathbf{t}^{(r)} = \mathbf{t}_d^{(r)} + \frac{\Theta \mathbf{Z}^{(r)} + i\omega\tau\kappa_f \mathbf{X}^{(r)}}{1 + i\omega\gamma^{(r)}\tau},$$
(28)

where

$$\mathbf{X}^{(r)} = \mathbf{t}_d^{(r)} : \mathbf{S}^{(0)} : (\mathbf{I}_2 \otimes \mathbf{I}_2) : \mathbf{S}^{(0)} : \mathbf{t}_d^{(r)},$$

$$\mathbf{Z}^{(r)} = \mathbf{t}_d^{(r)} : \mathbf{S}^{(0)} : (\mathbf{I}_2 \otimes \mathbf{I}_2) : \mathbf{S}^{(0)} : (\sum_{r=1}^{N_c} \frac{v^{*(r)}\mathbf{t}_d^{(r)}}{1+i\omega\gamma^{(r)}\tau}),$$

$$\Theta = \kappa_f \left\{ (1 - \kappa_f \mathbf{S}_{uuvv}^{(0)}) \left(\sum_{r=1}^{N_c} \frac{v^{*(r)}}{1 + i\omega\gamma^{(r)}\tau} \right) \right.$$
$$\left. + \kappa_f \left(\sum_{r=1}^{N_c} \frac{v^{*(r)}(\mathbf{K}_d^{(r)})_{uuvv}}{1 + i\omega\gamma^{(r)}\tau} \right) - \frac{ik_u k_v \Gamma_{uv}\kappa_f}{\eta_f \omega} \right\}^{-1},$$

and $\gamma^{(r)} = 1 + \kappa_f (\mathbf{K}_d^{(r)} - \mathbf{S}^{(0)})_{uuvv}$.

Here, ω is the frequency; τ is the relaxation time constant; κ_f and η_f are the bulk modulus and viscosity of the fluid, respectively; k_u and k_v are components of the wavenumber vector; Γ_{uv} is the component of the permeability tensor of the rock and the subscripts u and v represent summation over u and v, respectively ($u,v = 1,2,3$); and finally $v^{*(r)} = v^{(r)}\varphi_1$.

MODELING OF CEMENTATION MODELS

Here we discuss some results obtained using the CIM for simulating various cementation effects. The initial procedure is to find a pore model that calibrates the elastic parameters to those considered before compaction occurs. Subsequently, various cementation scenarios are modeled by adding cement into the various pore geometries in different ways. For the modeling we consider porous quartz sandstone, which, for simplicity, has a

pore structure defined by four aspect ratios and corresponding concentrations that in this case represent the spectrum of stiff to compliant pores. The permeability is 50 mD and the relaxation time constant is set to 10^{-7} s^{-1}. The details of the model can be found in Tables 1 and 2. To adapt to a granular structure, we set the total porosity without cement to 30%.

Figure 5 illustrates various models in which cement is gradually filling the pore space but the geometrical details of the

Table 1. Aspect ratios and concentrations of the inclusions used for modeling various cementation models. The total porosity is 30%.

Aspect ratio	Concentration
1.000	0.25294
0.100	0.04200
0.010	0.00460
0.001	0.00046

Table 2. Properties of the minerals and fluid used in the modeling (compiled from Mavko et al., 2009).

	Bulk modulus (GPa)	Shear modulus (GPa)	Density (kg/m^3)
Quartz	37.0	44.0	2650
Clay 1	21.0	7.0	2600
Clay 2	1.5	1.4	1580
Water	2.2	0.0	1000
NaCl	24.9	14.7	2163

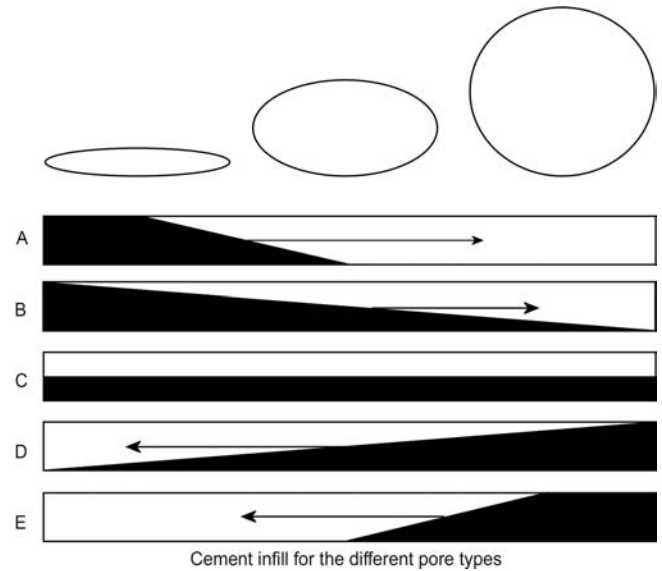Cement infill for the different pore types

Figure 5. Various cementation models in which the cement infill (black) depends on the pore type. From cementation model A–E, the cement infill progress from compliant pores toward spherical pores until all of the pores are filled.
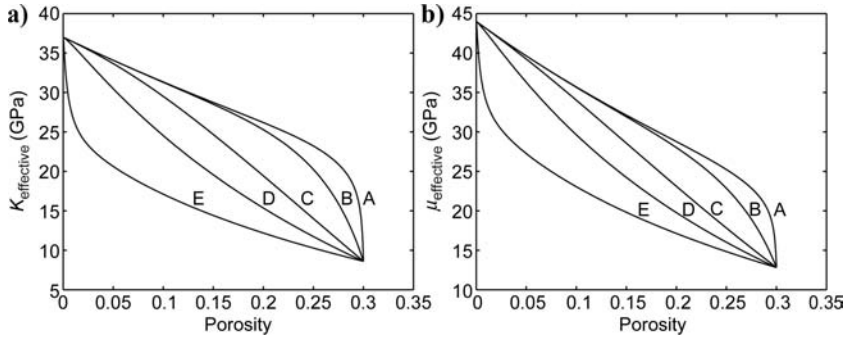
Figure 6. Effective bulk modulus (a) and shear modulus (b) as functions cement infill considering various cementation models. Cement is quartz.
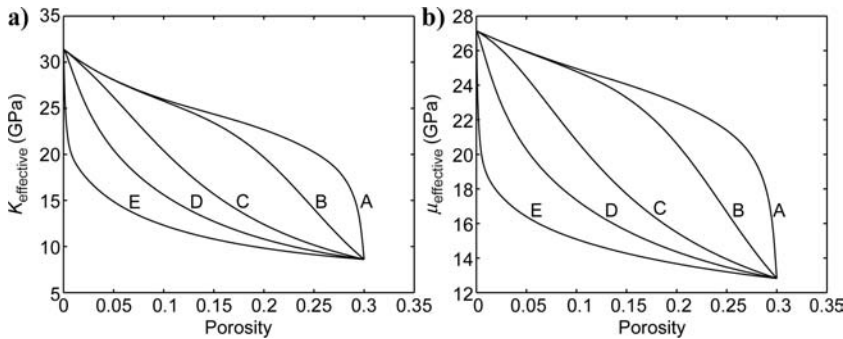

Figure 7. Effective bulk modulus (a) and shear modulus (b) as functions cement infill considering various cementation models. Cement is stiff clay (clay 1).
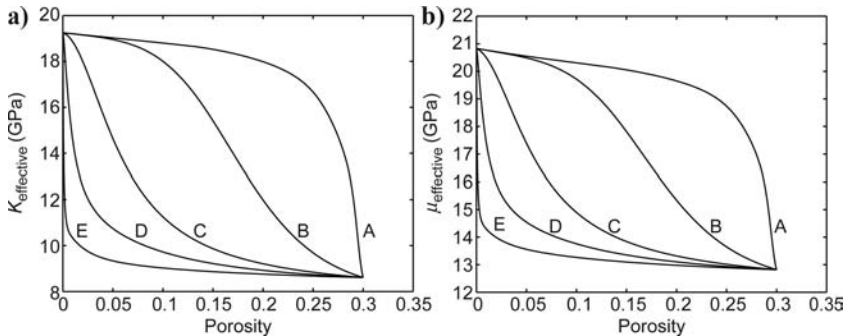

Figure 8. Effective bulk modulus (a) and shear modulus (b) as functions cement infill considering various cementation models. Cement is soft clay (clay 2).
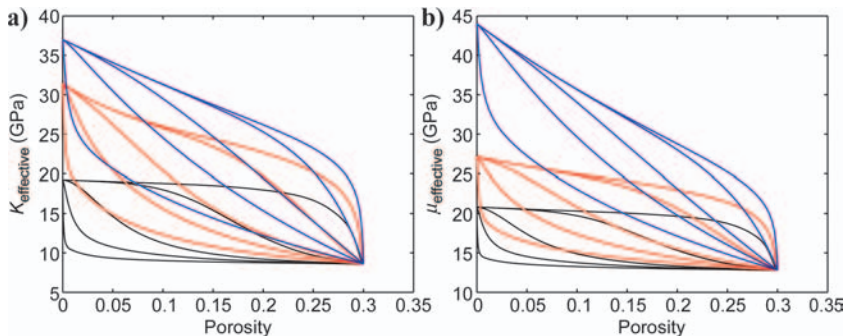

Figure 9. Comparison of effective bulk modulus (a) and shear modulus (b) as functions of cement infill considering various cementation models and cement properties. Cement: quartz (blue), stiff clay (red), and soft clay (black).

cement distributions vary. Five cement distributions are considered, labeled A–E in the figure. In model A, the cement first gradually fills into the most compliant pores (of smallest aspect ratio, i.e., α_4); when these are fully cemented, infill starts in pores of aspect ratio α_3, and so forth. The other extreme model E illustrates the opposite situation in which the cementation starts in the stiff and spherical pores (α_1), followed by cementation of pores of a lesser aspect ratio α_2, and so forth. The remaining models B–D represent intermediate models in which B is close to A, D is close to E, and C implies the same cementation in all pore types.

Figures 6–8 show the modeled bulk and shear moduli for all five distribution models, in which the stiffness parameters of the cement are varied; that is, Figure 6, quartz; Figure 7, clay 1 (stiff); and Figure 8, clay 2 (soft) (see Table 2). The curves reveal that upper elastic bounds of the five scenarios are obtained when compliant pores are cemented first (A), whereas lower elastic bounds of the five scenarios occur when the spherical pores are cemented first (E). For a better comparison, all of the modeled curves are plotted in Figure 9. It shows that softening the cement reduces the effective elastic parameters in general. Thus, the strong stiffening effect caused by any cement at grain contacts (distribution model A), as predicted by the CCT model, is also seen here. In Figure 10, we have, for comparison, included the Hashin–Shtrikman upper and lower bounds (Hashin and Shtrikman, 1963) with end members taken at the mineral point. The CCT (Dvorkin and Nur, 1996) is also plotted. In this comparison we have calibrated the CCT to model the elastic moduli at the critical porosity point, at which there is no cement in the pores. For CCT and Hashin–Shtrikman bounds at critical porosity, the bulk and shear modulus are 8.61 and 12.82 GPa, respectively. The cement distribution D can be viewed as equivalent to the friable sand model (Dvorkin and Nur, 1996), and interpolation curves made from these two extreme curves can moreover be associated with various sorting of the sand and thus expose similar properties as the constant cement model of Avseth et al. (2000) (Figure 10). Note that the distribution E, which corresponds to the spherical pores cemented first, represents an extreme case and is unlikely to be observed in nature. Thus, the distribution E may be regarded as a theoretical lower bound. In our numerical modeling, we have only considered three different, rather arbitrarily chosen, cement distribution models within the distributions (A and E). In practice, these should be tuned to adapt to real scenarios.

In Figures 11 and 12, we further test our modeling on a limited set of laboratory data in which salt cementation of three sandstone

samples has been studied (T. Vanorio, personal communication, 2010). Here V_P and V_S are measured for three samples of 6.3%, 10.2% and 17.5% porosity. The velocities were first measured at dry conditions (blue dots). The samples were then fully brine-saturated and subsequently dried to let salt precipitate within the pore space. The black dots show the measurements of the salt-cemented samples. A scanning electron microscopy (SEM) image before and after the salt precipitation for one of the samples can be found in Figure 13. To test our modeling, we first calibrated measured and modeled data points at the initial dry conditions by trial and error, perturbing the pore model until a good fit was obtained (Table 3). Because the pore spectrum of the samples was unknown, we limited our calibration to have as few (and stiff) pores as possible. To obtain a good fit for the P- and S-velocities for the three samples, 15% of the pores in samples S1 and S3 and 25% of the pores in sample S2 were horizontally aligned. Formally, this implies that the samples behave elastically slightly anisotropic, but this was not scrutinized any further. Thereafter, the effects of salt with the properties listed in Table 2 cementing the pore space in different ways (A–E) were tested. A good match was obtained for samples S1 and S2, when the salt is assumed to precipitate at grain contacts (i.e., filling the compliant pores first [A]). For sample S3, the best match indicates an even cement distribution (C).

Frequency dependence of seismic properties is usually caused by pore fluid dynamics, which occur when the pore volume is strained because of the impact of a seismic wave. The magnitudes of the dispersion effects are governed by the viscosity of the pore fluid and the topology (and compressibility) of the pore space. In particular, the connectivity between pores influences the permeability and the fluid flow behavior. Because the pore structure can vary with cementation, this can also affect the frequency dispersion. To illustrate this, we consider two cases in which the cementation performs differently. In case 1, we assume cement compliant pores are cemented first (A), whereas in case 2, the voids are cemented first (E).
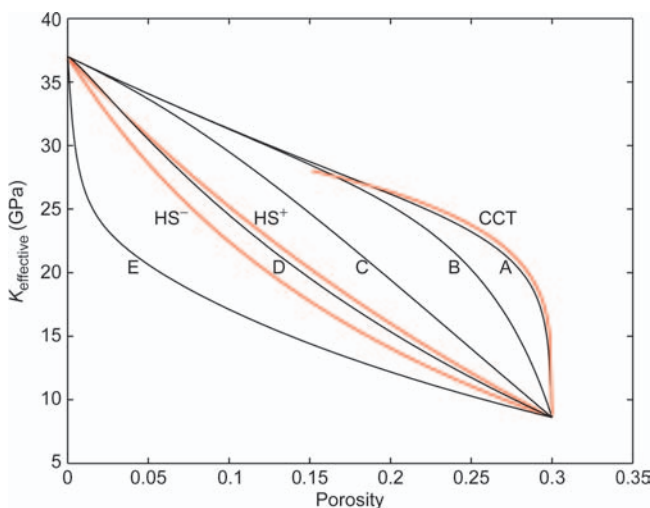
Figure 14 shows the modeled bulk modulus versus frequency for various porosities considering case 1. We see that for the highest porosity point (black curve), the frequency dispersion is substantial. With decreasing porosity due to cementation, the compliant and flat pores become fully cemented and the dispersion vanishes. Hence, as the remaining open porosity becomes gradually void-like, the critical frequency increases, which means that even for higher frequencies typically used in laboratory experiments, the elastic behavior remains consistent with that predicted by Gassmann (1951). Cementation considering case 2 produces the open porosity to be made up of an increasing amount of flat pores, which makes the dispersion become more prominent, as seen in Figure 15. Consequently, our modeling indicates that where the cement precipitates (grain contacts versus voids) also influences the frequency dispersion characteristics of the sediment. In Figures 14 and 15, the reduction in porosity due to cementation between each successive curve is 5% with an initial porosity of 30%.
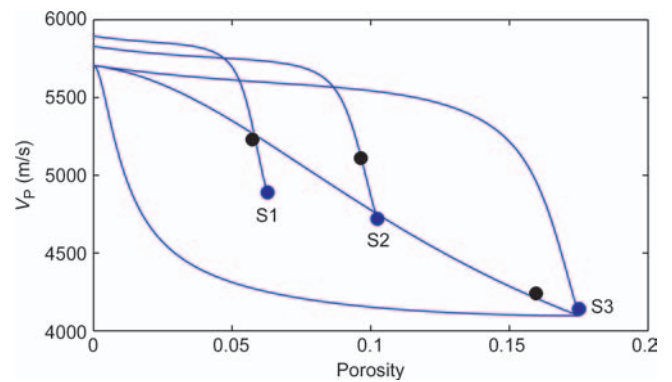

Figure 11. Measured dry P-velocities of three sandstone samples before (blue) and after (black) salt is precipitated in the pores. Solid lines are the modeled data using various cementation models. For samples S1 and S2, cementation model A is used; for sample S3, cementation model C is used. The data are provided by T. Vanorio (personal communication, 2010).

Figure 12. Measured dry S-velocities of three sandstone samples before (blue) and after (black) salt is precipitated in the pores. Solid lines are the modeled data using various cementation models. For samples S1 and S2, cementation model A is used; for sample S3, cementation model C is used. The data are provided by T. Vanorio (personal communication, 2010).
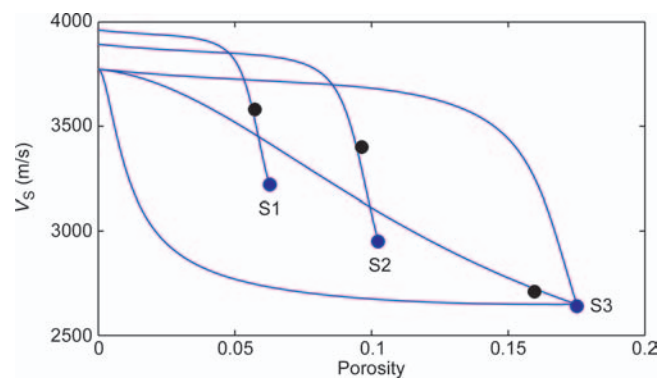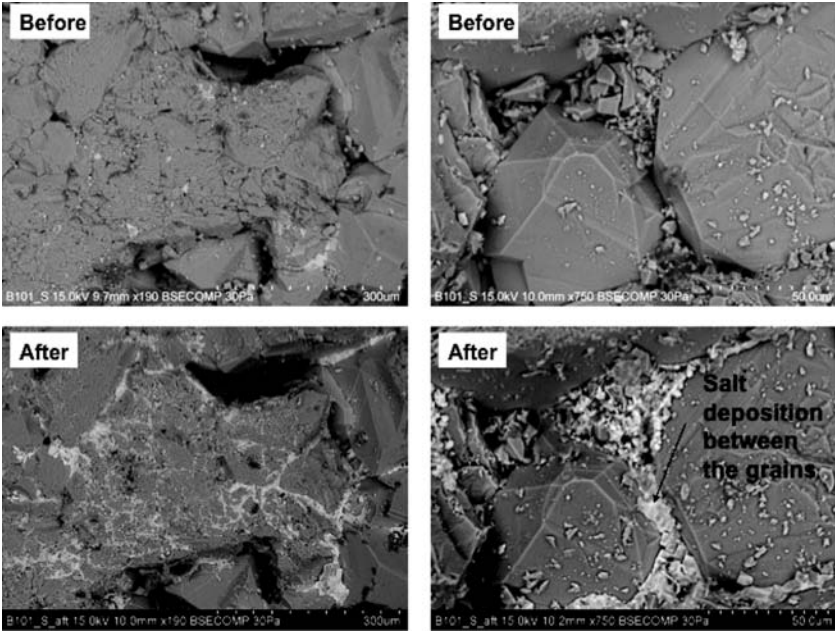

Figure 10. Comparison of various cementation models. Here, HS^- and HS^+ denote the lower and upper Hashin–Shtrikman bounds, respectively. Here, HS^- is equivalent to the friable sand model of Dvorkin and Nur (1996).

Figure 13. SEM images before and after salt precipitation. Images compiled from Vanorio et al. (2010).

Table 3. The aspect ratios and concentrations of the inclusions used for modeling samples S1, S2, and S3.

Sample S1		Sample S2		Sample S3	
Aspect ratio	Concentration	Aspect ratio	Concentration	Aspect ratio	Concentration
1.000	0.0508	1.0000	0.0884	1.000	0.1541
0.025	0.0040	0.0250	0.0040	0.025	0.0120
0.010	0.0080	0.0100	0.0100	0.010	0.0100

DISCUSSION

The aim of this paper is first and foremost to present an alternative approach for the modeling of compaction effects on elastic and seismic properties of siliciclastic rocks. One main advantage of this model is that local heterogeneities in the composition on the grain scale can be directly taken into account (e.g., differences in the cement and grain properties). Thus, the procedure does not imply modeling of a set of effective elastic properties of the mineral phase before the inclusions are embedded. However, this is also a feature of the model of Dvorkin and Nur (1996). Another advantage is that there is no limitation in the amount of cement to fill the pore space. This means that the modeling of elasticity effects due to a transition from contact to pore-filling cement does not require any hybrid technique, as is the case for the approach of Dvorkin et al. (1999). Here, this transition is described by altering the modeling from using CCT to an inclusion-based model. Furthermore, because attenuation and dispersion effects are modeled, our rock physics model can be formally calibrated to low- and/or high-frequency data. In fact, the calibration of pore structure parameters should essentially improve if dispersion signatures are available.

The CIM should also be relevant for studying the seismic properties of carbonates because it is flexible with respect to defining pore structure properties and connectivity between pores. Controlled pore fluid substitution experiments in carbonates have also shown that the shear modulus can be altered (Assefa et al., 2003; Baechle et al., 2005; Rossebø et al., 2005;
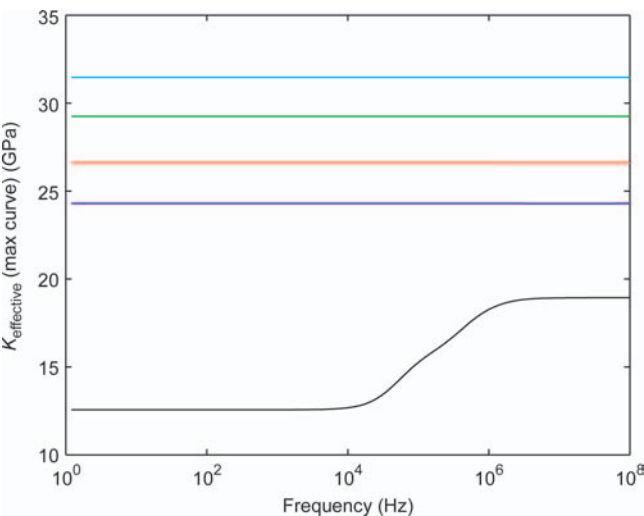

Figure 14. The modeled effective bulk modulus versus frequency for different porosity values in which the cement infill starts at a porosity of 0.3 and subsequent cementation closes the compliant pores first (cementation model A). Porosity values: 0.30 (black), 0.25 (blue), 0.20 (red), 0.15 (green), and 0.10 (cyan).
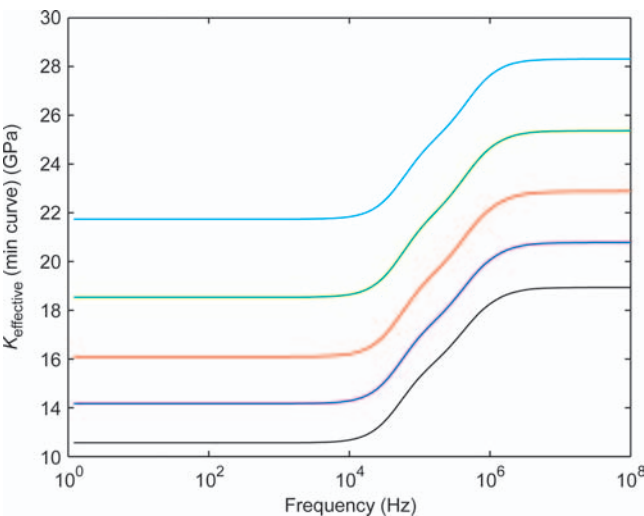

Figure 15. The modeled effective bulk modulus versus frequency for different porosity values in which the cement infill starts at a porosity of 0.3 and subsequent cementation closes the stiff pores first (cementation model E). Porosity values: 0.30 (black), 0.25 (blue), 0.20 (red), 0.15 (green), and 0.10 (cyan).

Adam et al., 2006; Agersborg et al., 2008; Vanorio et al., 2008), which violates the assumption for the direct use of the Gassmann model (Gassmann, 1951) even if the pore space is fully connected. With our approach, combined effects of weakening or stiffening of the pore walls by altering the elastic properties of shells surrounding the pore and dispersion due to pore fluid flow can be investigated. However, this remains to be tested.

A main objection to the present model, and to all inclusion-based models, is the relatively large number of parameters needed to be set for its use. Moreover, many of the model parameters are defined to obtain a mathematical formulation for the overall elastic moduli. As such, the rock physics parameters needed are more mathematically founded than representing a true physical model. This fact also makes the model somewhat difficult to verify from experimental data because rock physics parameters, which cannot be directly accessed from the sample itself (so-called fuzzy parameters), can be perturbed until a best-fit solution between modeled and observed data is obtained. However, at this stage the model can still be utilized to understand various effects on seismic parameters due to altered composition or physical conditions.

CONCLUSIONS

We have presented a CIM as a framework for modeling cementation effects on elastic properties of siliciclastic sediments. The rock is considered as a continuous elastic material embedding coated inclusions. The inclusions consist of a kernel associated with the pore, which is surrounded by coatings or shells that define the cementing material. The inclusions and pores can have different pore aspect ratios, which yields the possibility of the cement occupying the various types of pores in different ways.

The main result of this paper is the formal presentation of the model itself. Thus, our numerical experiments are seen to qualitatively agree well with results obtained using other rock physics models considering cementation effects. The model allows for the possibility of including small-scale heterogeneities in rock physics modeling, which thereby enhances our capability to link details about the sedimentology to physical properties. As such, this allows for a closer integration of geologic and geophysical properties. Because the heterogeneities focused on in this paper can be related to reservoir quality, the model should also be relevant for reservoir characterization from seismic data.

ACKNOWLEDGMENTS

APPENDIX A

COMPUTING THE CONCENTRATION TENSOR β

To find the interaction tensor $\boldsymbol{\beta}^{(j)}$ for the t-matrix of family r, we follow the derivation of Lipinski et al. (2006). By starting with two adjacent layers j and $j + 1$, which have a perfect bounding in an inclusion, the displacement and traction vectors are continuous at the interface. At any point on the interface a relation between strain and stresses can be established as proven by Hill (1972) and

Walpole (1978). The strain through the interface can be written as (Walpole, 1981; Lipinski, 2006)

$$\boldsymbol{\varepsilon}_{j+1}^{(r)}(\mathbf{x}) - \boldsymbol{\varepsilon}_j^{(r)}(\mathbf{x}) = \mathbf{P}(\mathbf{C}^{(j+1)}) : (\mathbf{C}^{(j)} - \mathbf{C}^{(j+1)}) : \boldsymbol{\varepsilon}_j^{(r)}(\mathbf{x}).$$
(A-1)

Here, $\mathbf{P}(\mathbf{C}^{(j+1)})$ is the interfacial operator defined as $P_{ijk\ell}(\mathbf{C}^{(j+1)}) = -G_{ijk\ell}(\mathbf{C}^{(j+1)})$.

By rearranging equation A-1, we obtain

$$\boldsymbol{\varepsilon}_{j+1}^{(r)}(\mathbf{x}) = (\mathbf{I}_4 + \mathbf{G}(\mathbf{C}^{(j+1)}) : (\mathbf{C}^{(j+1)} - \mathbf{C}^{(j)})) : \boldsymbol{\varepsilon}_j^{(r)}(\mathbf{x}),$$
(A-2)

which relates the strain from layer $j + 1$ to layer j.

The goal is to find the average strain of the inclusion r. By starting with the kernel, we can find the average strain field in the first coating (subscript 2) related to the strain field in the kernel (subscript 1) as

$$\boldsymbol{\varepsilon}_2^{(r)} = (\mathbf{I}_4 + \mathbf{G}^{(2)} : (\mathbf{C}^{(2)} - \mathbf{C}^{(1)})) : \boldsymbol{\varepsilon}_1^{(r)}.$$
(A-3)

Here, $\mathbf{G}^{(2)}$ is defined as

$$\mathbf{G}^{(2)} = -\frac{1}{|V_2^{(r)}|} \int_{V_2^{(r)}} d\mathbf{x} \mathbf{G}(\mathbf{C}^{(2)})$$
(A-4)

and Cherkaoui et al. (1994) and Lipinski et al. (2006) have shown that $\mathbf{G}^{(2)}$ can be written as

$$\mathbf{G}^{(2)} = \mathbf{G}^{(V_1^{(r)})}(\mathbf{C}^{(2)}) - \frac{\phi_1}{\phi_2}(\mathbf{G}^{(V_1^{(r)}+V_2^{(r)})}(\mathbf{C}^{(2)}) - \mathbf{G}^{(V_1^{(r)})}(\mathbf{C}^{(2)})).$$
(A-5)

Inserting equation A-5 into equation A-3, we obtain

$$\boldsymbol{\varepsilon}_2^{(r)} = \left(\mathbf{I}_4 + \left[\mathbf{G}^{(V_1^{(r)}+V_2^{(r)})}(\mathbf{C}^{(2)}) + \frac{\phi_1}{\phi_2}(\mathbf{G}^{(V_1^{(r)}+V_2^{(r)})}\right.\right.$$
$$\left.\left. \times (\mathbf{C}^{(2)}) - \mathbf{G}^{(V_1^{(r)})}(\mathbf{C}^{(2)}))\right] : (\mathbf{C}^{(2)} - \mathbf{C}^{(1)})\right) : \boldsymbol{\varepsilon}_1^{(r)},$$
(A-6)

which may be simplified by introducing the tensor $\boldsymbol{\chi}$ such that

$$\boldsymbol{\varepsilon}_2^{(r)} = \boldsymbol{\chi}^{(2/1)} : \boldsymbol{\varepsilon}_1^{(r)},$$
(A-7)

$$\boldsymbol{\varepsilon}_1^{(r)} = \boldsymbol{\beta}^{(1)} : \boldsymbol{\varepsilon}^{(r)},$$
(A-8)

and

$$\boldsymbol{\varepsilon}_2^{(r)} = \boldsymbol{\chi}^{(2/1)} : \boldsymbol{\beta}^{(1)} : \boldsymbol{\varepsilon}^{(r)},$$
(A-9)

which we can be written as

$$\boldsymbol{\varepsilon}_2^{(r)} = \boldsymbol{\beta}^{(2)} : \boldsymbol{\varepsilon}^{(r)}.$$
(A-10)

Here, $\boldsymbol{\beta}^{(2)} = \boldsymbol{\chi}^{(2/1)} : \boldsymbol{\beta}^{(1)}$.

If we extend to one more coating, the strain in coating 3 will be, according to equation A-2,

$$\boldsymbol{\varepsilon}_3^{(r)} = \frac{\varphi_1}{\varphi_1 + \varphi_2}(\mathbf{I}_4 + \mathbf{G}(\mathbf{C}^{(3)}) : (\mathbf{C}^{(3)} - \mathbf{C}^{(1)})) : \boldsymbol{\varepsilon}_1^{(r)}$$
$$+ \frac{\varphi_2}{\varphi_1 + \varphi_2}(\mathbf{I}_4 + \mathbf{G}(\mathbf{C}^{(3)}) : (\mathbf{C}^{(3)} - \mathbf{C}^{(2)})) : \boldsymbol{\varepsilon}_2^{(r)}.$$
(A-11)

By comparing equation A-6 with equation A-11, the $\boldsymbol{\chi}$ tensor for the third coating can be expressed as

$$
\boldsymbol{\chi}^{(3/j)} = \mathbf{I}_4 + \left[\mathbf{G}^{(V_1^{(r)}+V_2^{(r)})}(\mathbf{C}^{(3)}) + \frac{\phi_1 + \phi_2}{\phi_3} \right.
$$
$$
\left. \times \; (\mathbf{G}^{V_1^{(r)}+V_2^{(r)}+V_3^{(r)}}(\mathbf{C}^{(3)}) - \mathbf{G}^{(V_1^{(r)}+V_2^{(r)})}(\mathbf{C}^{(3)})) \right] :
$$
$$
\times \; (\mathbf{C}^{(3)} - \mathbf{C}^{(j)}), \tag{A-12}
$$

and equation A-11 can be simplified to

$$
\boldsymbol{\varepsilon}_3^{(r)} = \left(\frac{\varphi_1}{\varphi_1 + \varphi_2} \boldsymbol{\chi}^{(3/1)} + \frac{\varphi_2}{\varphi_1 + \varphi_2} \boldsymbol{\chi}^{(3/2)} : \boldsymbol{\chi}^{(2/1)} \right) : \boldsymbol{\beta}^{(1)} : \boldsymbol{\varepsilon}^{(r)}. \tag{A-13}
$$

The concentration tensor for the third coating can then be written as

$$
\boldsymbol{\beta}^{(3)} = \left(\frac{\varphi_1}{\varphi_1 + \varphi_2} \boldsymbol{\chi}^{(3/1)} + \frac{\varphi_2}{\varphi_1 + \varphi_2} \boldsymbol{\chi}^{(3/2)} : \boldsymbol{\chi}^{(2/1)} \right) : \boldsymbol{\beta}^{(1)}, \tag{A-14}
$$

and by introducing the tensor $\boldsymbol{\Lambda}$ such that

$$
\boldsymbol{\Lambda}^{(1)} = \mathbf{I}_4 \tag{A-15}
$$

and

$$
\boldsymbol{\Lambda}^{(2)} = \boldsymbol{\chi}^{(2/1)}, \tag{A16}
$$

we can further simplify the interaction tensor for the third coating as

$$
\boldsymbol{\beta}^{(3)} = \boldsymbol{\Lambda}^{(3)} : \boldsymbol{\beta}^{(1)}. \tag{A-17}
$$

Here

$$
\boldsymbol{\Lambda}^{(3)} = \left(\frac{\phi_1}{\phi_1 + \phi_2} \boldsymbol{\chi}^{(3/1)} + \frac{\phi_2}{\phi_1 + \phi_2} \boldsymbol{\chi}^{(3/2)} : \boldsymbol{\chi}^{(2/1)} \right)
$$
$$
= \frac{\sum_{j=1}^{2} \phi_j \boldsymbol{\chi}^{(3/j)} : \boldsymbol{\Lambda}^{(j)}}{\sum_{j=1}^{2} \phi_j}. \tag{A-18}
$$

For the next coating we follow the same procedure as delineated above, in which the strain of the $j+1$ coating is expressed by the previous kernel and coatings. For the $j+1$ coating, we have the following iterative equations:

$$
\boldsymbol{\beta}^{(j+1)} = \boldsymbol{\Lambda}^{(j+1)} : \boldsymbol{\beta}^{(1)}, \tag{A-19}
$$

$$
\boldsymbol{\Lambda}^{(j+1)} = \frac{\sum_{m=1}^{j} \phi_m \boldsymbol{\chi}^{(j+1/m)} : \boldsymbol{\Lambda}^{(m)}}{\sum_{m=1}^{j} \phi_m}, \tag{A-20}
$$

$$
\boldsymbol{\chi}^{(j+1/m)} = \mathbf{I}_4 + \left[\mathbf{G}^{(V_1^{(r)}+\cdots+V_{j+1}^{(r)})}(\mathbf{C}^{(j+1)}) - \frac{\sum_{\ell=1}^{j} \phi_l}{\phi_{\ell+1}} \right.
$$
$$
\left. \times (\mathbf{G}^{(V_1^{(r)}+\cdots+V_{j+1}^{(r)})}(\mathbf{C}^{(j+1)}) - \mathbf{G}^{(V_1^{(r)}+\cdots+V_j^{(r)})}(\mathbf{C}^{(j+1)})) \right] :
$$
$$
\times (\mathbf{C}^{(j+1)} - \mathbf{C}^{(m)}), \tag{A-21}
$$

$$
\langle \boldsymbol{\beta}^{(j)} \rangle = \sum_{\ell=1}^{j} \phi_l \boldsymbol{\beta}^{(j)} = \mathbf{I}_4, \tag{A-22}
$$

and

$$
\boldsymbol{\beta}^{(1)} = \left(\sum_{j=1}^{k} \phi_j \boldsymbol{\Lambda}^{(j)} \right)^{-1}. \tag{A-23}
$$

Hence, by starting with the kernel of the multicoated inclusion it is possible by iteration to find every interaction tensor for the inclusion containing k layers of coating to be subsequently used in the t-matrix equations.

REFERENCES

Adam, L., M. Batzle, and I. Brevik, 2006, Gassmann's fluid substitution and shear modulus variability in carbonates at laboratory seismic and ultrasonic frequencies: Geophysics, **71**, no. 6, F173–F183, doi:10.1190/1.2358494.

Agersborg, R., T. A. Johansen, M. Jakobsen, J. Sothcott, and A. Best, 2008, Effect of fluids and dual-pore systems on pressure-dependent velocities and attenuations in carbonates: Geophysics, **73**, no. 5, N35–N47.

Assefa, S., C. McCann, and J. Sothcott, 2003, Velocities of compressional and shear waves in limestones: Geophysical Prospecting, **51**, 1–13, doi:10.1046/j.1365-2478.2003.00349.x.

Avseth, P., J. Dvorkin, G. Mavko, and J. Rykkje, 2000, Rock physics diagnostics of North Sea sand: Link between microstructure and seismic properties: Geophysical Research Letters, **27**, 2761–2764, doi:10.1029/1999GL008468.

Avseth, P., T. Mukerji, and G. Mavko, 2005, Quantitative seismic interpretation: Applying rock physics tools to reduce interpretation risk: Cambridge University Press.

Baechle, G. T., R. J. Weger, G. P. Eberli, J.-L. Massafferro, and Y.-F. Sun, 2005, Changes of shear moduli in carbonate rocks: Implications for Gassmann applicability: The Leading Edge, **24**, 507–510, doi:10.1190/1.1926808.

Cherkaoui, M., H. Sabar, and M. Berveiller, 1994, Micromechanical approach of the coated inclusion problem and application to composite-materials: Journal of Engineering Materials and Technology, **116**, 274–278, doi:10.1115/1.2904286.

Dræge, A., M. Jakobsen, and T. A. Johansen, 2006a, Rock physics modelling of shale diagenesis: Petroleum Geoscience, **12**, 49–57, doi:10.1144/1354-079305-665.

Dræge, A., T. A. Johansen, I. Brevik, and C. Thorsen Dræge, 2006b, A strategy for modelling diagenetic evolution of seismic properties in sandstones: Petroleum Geoscience, **12**, no. 4, 309–323, doi:10.1144/1354-079305-691.

Dvorkin, J., J. Berryman, and A. Nur, 1999, Elastic moduli of cemented sphere packs: Mechanics of Materials, **31**, 461–469, doi:10.1016/S0167-6636(99)00009-5.

Dvorkin, J., and A. Nur, 1996, Elasticity of high-porosity sandstone: Theory for two North Sea datasets: Geophysics, **61**, 1363–1370, doi:10.1190/1.1444059.

Dvorkin, J., A. Nur, and H. Yin, 1994, Effective properties of cemented granular material: Mechanics of Materials, **18**, 351–366, doi:10.1016/0167-6636(94)90044-2.

Gassmann, F., 1951, Über die elastizität poröser medien: Vierteljahrschrift der Naturforschende Gesellschaft in Zürich, **96**, 1–23.

Hashin, Z., and S. Shtrikman, 1963, A variational approach to the theory of the elastic behaviour of multiphase materials: Journal of the Mechanics and Physics of Solids, **11**, 127–140, doi:10.1016/0022-5096(63)90060-7.

Hill, R., 1972. An invariant treatment of interfacial discontinuities in elastic composites, *in* L. I. Sedov, ed., Continuum mechanics and related problems of analysis, 597–604.

Jakobsen, M., and M. Chapman, 2009, Unified theory of global flow and squirt flow in cracked porous media: Geophysics, **74**, no. 2, WA65–WA76, doi:10.1190/1.3078404.

Jakobsen, M., J. A. Hudson, and T. A. Johansen, 2003a, T-matrix approach to shale acoustic: Geophysical Journal International, **154**, 533–558, doi:10.1046/j.1365-246X.2003.01977.x.

Jakobsen, M., and T. A. Johansen, 2005, The effect of drained and undrained loading on visco-elastic waves in rock-like composites: International Journal of Solids and Structures, **42**, 1597–1611, doi:10.1016/j.ijsolstr.2004.07.016.

Jakobsen, M., T. A. Johansen, and C. McCann, 2003b, The acoustic signature of fluid flow in complex porous media: Journal of Applied Geophysics, **54**, 219–246, doi:10.1016/j.jappgeo.2002.11.004.

Johansen, T. A., B. Ole Ruud, and M. Jakobsen, 2004, Effect of grain scale alignment on seismic anisotropy and reflectivity of shales: Geophysical Prospecting, **52**, 133–149, doi:10.1046/j.1365-2478.2003.00405.x.

Lipinski, P., E. H. Barhdadi, and M. Cherkaoui, 2006, Micromechanical modeling of an arbitrary elliposoidal multi-coated inclusion: Philosophical Magazine, **86**, 1305–1326, doi:10.1080/14786430500343868.

Mavko, G., T. Mukerji, and J. Dvorkin, 2009, The Rock physics handbook: Tools for seismic analysis in porous media: Cambridge University Press.

Rossebø, Ø. H., I. Brevik, G. R. Ahmadi, and L. Adam, 2005, Modeling of acoustic properties in carbonate rocks: 75th Annual International Meeting, SEG, Expanded Abstracts, 1505–1508.

Sayers, C. M., and M. Kachanov, 1995, Microcrack-induced elastic wave anisotropy of brittle rocks: Journal of Geophysical Research, **100**, 4149–4156, doi:10.1029/94JB03134.

Vanorio, T., G. Mavko, and S. Vialle, 2010, The rock physics basis for 4D seismic monitoring of CO_2 fate: Are we there yet?: The Leading Edge, **29**, 156–162.

Vanorio, T., C. Scotellaro, and G. Mavko, 2008, The effect of chemical and physical processes on acoustic properties of carbonate rocks: The Leading Edge, **27**, 1040–1048, doi:10.1190/1.2967558.

Walpole, L. J., 1978, A coated inclusion in an elastic medium: Mathematical Proceedings of the Cambridge Philosophical Society, **83**, 495–506, doi:10.1017/S0305004100054773.

——, 1981, Elastic behaviour of composite materials: Theoretical foundations: Advances in Applied Mechanics, **21**, 169–242, doi:10.1016/S0065-2156(08)70332-6.